University of Seville
Master in Nuclear Physics

Characterization of the ion pedestal in low and high collisionality plasmas

Diego José Cruz Zabala

Supervisor:
Eleonora Viezzer

Departamento de Física Atómica, Molecular y Nuclear

Facultad de Física

Resumen

El modo de alto confinamiento (H-mode) es un régimen muy importante para futuros dispositivos de fusión. En este régimen, el confinamiento global se incrementa y se desarrolla una estructura de pedestal en los perfiles. Sin embargo, todavía falta una comprensión completa de cómo es formado. En este régimen, el perfil de la velocidad toroidal de las impurezas presenta un mínimo local cerca de la última superficie de flujo magnético cerrada y, bajo ciertas condiciones, las impurezas en el borde del plasma pueden rotar en dirección opuesta comparada con el centro del plasma.

Una base de datos sobre el pedestal ha sido compilada con datos de ASDEX Upgrade para intentar progresar en la comprensión de la física del pedestal. Esta tesis está enfocada en el estudio del perfil de la temperatura iónica y del perfil de la velocidad toroidal de las impurezas, obtenidos con el sistema "charge exchange recombination spectroscopy", a baja y alta colisionalidad. La correlación entre las características del pedestal y el mínimo en la velocidad toroidal de las impurezas ha sido estudiada. Se ha observado que el mínimo en la velocidad toroidal de las impurezas alcanza valores negativos en descargas de baja colisionalidad, mientras que es positivo en descargas de alta colisionalidad. Además, la posición del mínimo de la velocidad toroidal de las impurezas está correlacionada con la posición de la parte superior de los pedestales de la temperatura iónica y densidad en descargas de alta colisionalidad, mientras que, para descargas de baja colisionalidad, solo está correlacionada con la posición de la parte superior del pedestal de la temperatura iónica.

Abstract

The high confinement mode (H-mode) is a very important regime for future fusion devices. In this regime, the global confinement is increased and a pedestal structure is developed in the profiles. However, a complete understanding of how it is formed is still missing. In this regime, the toroidal impurity velocity profile exhibits a local minimum close to the separatrix and, under certain conditions, the impurities at the plasma edge can rotate in the opposite direction compared to the plasma core.

A pedestal database was compiled with data from ASDEX Upgrade to try to progress in understanding the pedestal physics. This thesis is focussed on the study of the ion temperature and toroidal impurity velocity profiles, obtained with the charge exchange recombination spectroscopy system, at low and high collisionality. A correlation between the characteristics of the pedestal with the minimum in the toroidal impurity velocity was studied. It has been observed that the minimum in the toroidal impurity velocity reaches negative values in low collisionality discharges, while it is positive in high collisionality discharges. Moreover, the position of the minimum in the toroidal impurity velocity is correlated with the position of the ion temperature and density pedestal tops in high collisionality discharges, while it is only correlated with the position of the ion temperature pedestal top in low collisionality discharges.

Contents

Chapter 1

Introduction

1.1 Nuclear fusion

It is well known that the world's increasing energy consumption demands for new clean and abundant source of energy for the future. Fusion energy is one of the most prominent candidates to meet these demands. This kind of energy is produced in the Sun and in all the stars. The energy is obtained when two light nuclei fuse to a heavier one. In order to produce this reaction, the kinetic energy of the nuclei has to be high enough to overcome the Coulomb repulsion. Increasing the kinetic energy means increasing the temperature, which has to be of the order of hundreds of million of degrees in order that fusion can take place. At high temperatures a gas is fully ionized. This state of the matter is called plasma. The main characteristic of a plasma is that its kinetic energy is much higher than its potential energy. On Earth, the most prominent fusion reaction is between deuterium (D) and tritium (T), two isotopes of hydrogen (H):

$$^2D +\, ^3T \quad \rightarrow \quad ^4He + n + 17.6\ MeV \tag{1.1}$$
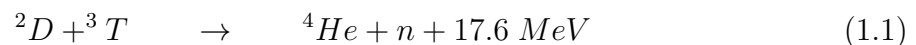
The high cross-section (see figure 1) and high energy yield makes the D-T reaction the most favourable one [1]. The products of the reaction are ^4He and neutrons. D is present in water. Approximately 0.015% of the hydrogen in ocean water is deuterium. However, T is not present in nature since it has half life of about 12 years. In order to produce T, the neutrons produced in the main fusion reaction are used to produce another reaction with lithium
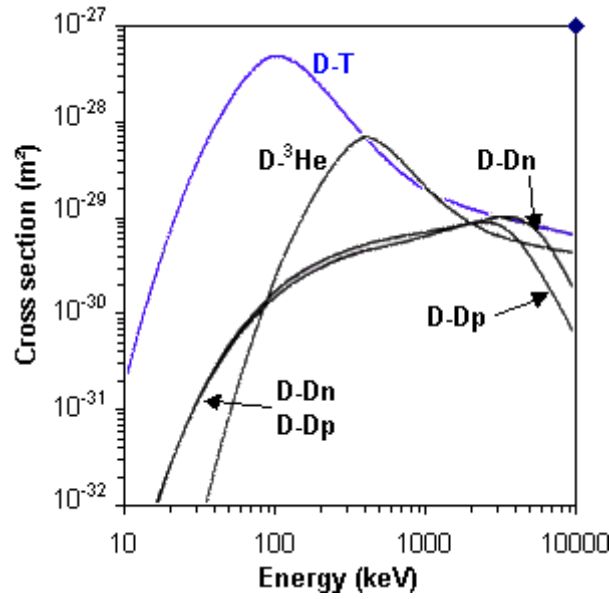
$$^6Li + n \quad \rightarrow \quad ^4He +\, ^3T + 4.8MeV \tag{1.2}$$
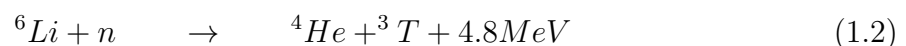
Figure 1.1: Rate coefficients for various fusion reactions.

1.2 Magnetic confinement and tokamak

In magnetic confinement fusion, the tokamak is one of the most developed concepts. Here, the plasma is confined in a toroidal geometry by magnetic fields. The schematic structure of the tokamak is shown in figure 1.2. The toroidal magnetic field, which is the dominant component of the total magnetic field, is created by toroidal field coils. In order to avoid loses due to particle drifts (see chapter 2.1), a poloidal magnetic field is created by a current in the plasma. This current is induced by a transformer coil. The sum of the toroidal and poloidal field produces a helical field as shown in figure 1.2. As the poloidal field is created by a transformer, the duration of each experiment in a tokamak is limited. Each experiment, also called plasma discharge, has a maximum duration which is determined by the characteristics of the transformer coil.

Figure 1.3 illustrates the coordinates used in a tokamak geometry. Here, r is the radial coordinate with origin in the plasma centre, R is the radial coordinate with origin in the torus centre, θ is the poloidal angle, ϕ is the toroidal angle, a is the minor radius and R_0 is the major radius. The results are usually represented as a function of the normalized poloidal flux coordinate ρ_{pol}, which is 0 at the plasma centre and 1 at the separatrix

$$\rho_{pol} = \sqrt{\frac{\Psi - \Psi_a}{\Psi_s - \Psi_a}} \tag{1.3}$$

where Ψ the 2D flux, Ψ_a is the flux at the plasma centre and Ψ_s is the flux at the separatrix. The flux surfaces are the constant magnetic flux surfaces (see figure 1.3). The
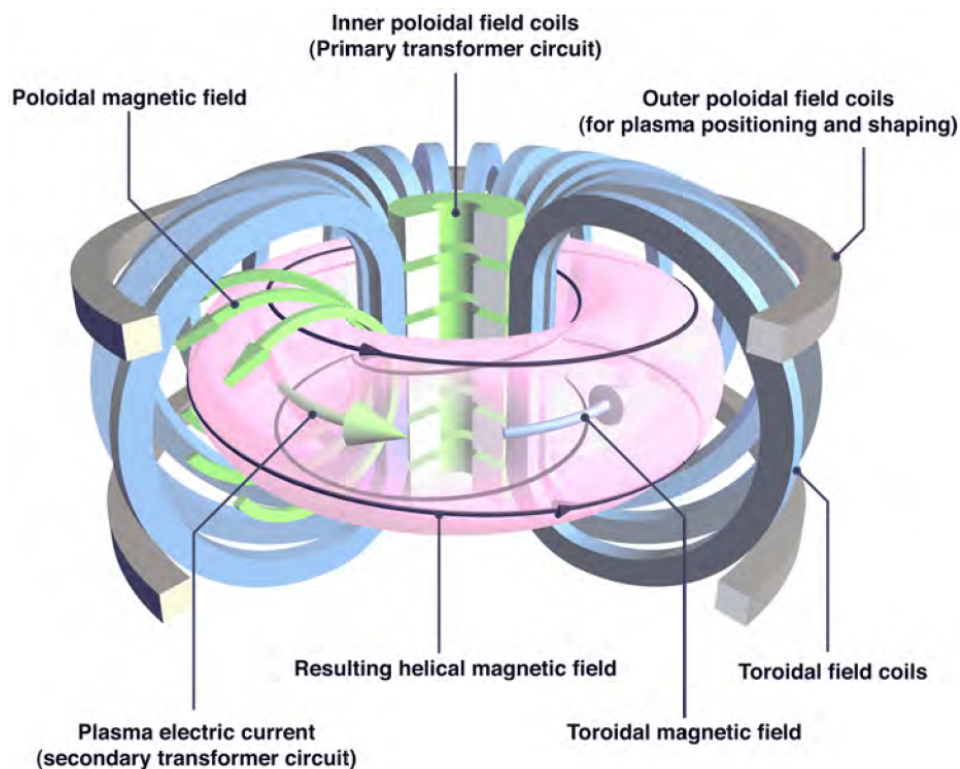
Figure 1.2: Schematic of a tokamak. Figure taken from [2].

separatrix is the last closed flux surface. The scrape of layer (SOL) is the region outside the separatrix.

To start the fusion reactions, the plasma has to be heated to temperatures of around tens of keV, which means hundreds of millions of degrees. There are two ways to heat the plasma to reach the conditions of fusion: injection of high energy neutral atoms and electromagnetic waves:

- **Neutral beam injection (NBI):** a beam of high energetic neutral atoms is injected into the plasma. These neutrals are ionized and heat the plasma via collisions.

- **Electromagnetic waves**: the waves are emitted to the plasma and, depending on their frequency, they heat the ions or the electrons. The system for heating the ions is called ICRH (Ion Cyclotron Resonance Heating) and for the electrons, ECRH (Electron Cyclotron Resonance Heating). In both cases, the species which is heated will also transfer part of the energy to the other species via collisions.

In a fusion power plant, the α particles generated by the fusion reactions heat the plasma.
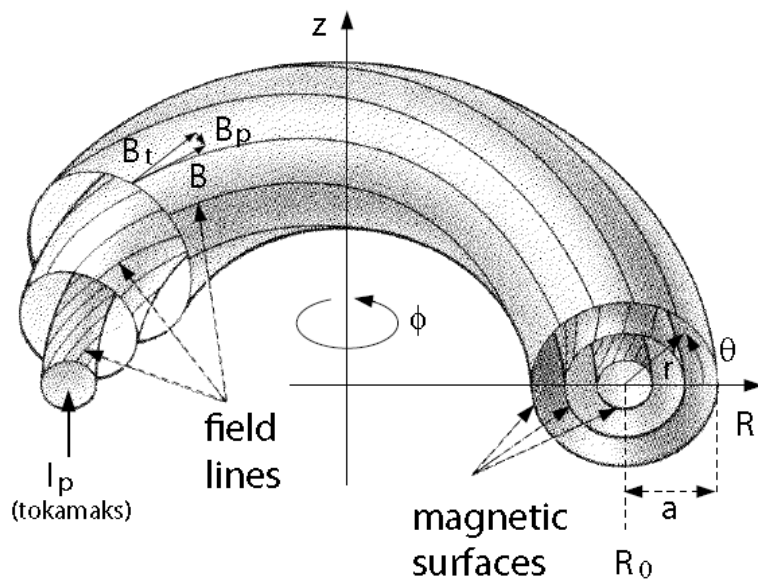
Figure 1.3: Schematic of the flux surfaces and the main coordinates in a tokamak.

major radius R_0	1.65 m
minor plasma radius a	0.5 m
plasma current I_p	0.4 - 1.2 MA
toroidal magnetic field B_ϕ	1.8 - 2.8 T
heating power P_{heat}	up to 30 MW
gas	D, H, He

Table 1.1: Typical parameters of AUG.

The Lawson criterion predicts the conditions to reach ignition:

$$n \cdot T \cdot \tau_E \geq 5 \cdot 10^{21} \, m^{-3} \cdot keV \cdot s \tag{1.4}$$

where T and n are the temperature and density of the plasma and τ_E is the energy confinement time.

The results presented in this thesis have been obtained in ASDEX Upgrade (AUG) tokamak, located at the Max-Planck-Institut für Plasmaphysik, Garching. The AUG tokamak is a divertor tokamak that started operation in 1991. The most important parameters of AUG are illustrated in table 1.1.

1.3 Goals

The discovery of the high confinement mode (H-mode) regime [3] implied a big improvement in the confinement of the plasma. The underlying physics behind the transition from the low confinement mode (L-mode) to the H-mode and the behaviour of the plasma in the H-mode is still unclear. The H-mode regime is characterized by the develop of a pedestal structure in the profiles. The pedestal is characterized by steep gradients over a few cm and an increase of temperature and density by 1-2 orders of magnitude. This causes typical lengths and times to change significantly on a small radial scale. The main goal of this work is to characterize the density and temperature profiles in the pedestal region. The profiles will be compared in H-mode plasmas with low and high collisionality. A database with measurements from the ASDEX Upgrade tokamak will be set up and correlations between density, temperature and other plasma parameters shall be identified. The database will include measurements in plasmas with deuterium, hydrogen and helium as main ion species as well as plasmas with external impurity seeding. The structure of the ion pedestal shall be compared to the electron pedestal. The impurity rotation reversal, observed at a certain collisionality threshold, will be examined in view of the identified dependencies.

Chapter 2

Theory overview

The high temperatures required such that fusion can take place could damage the machine if the interaction between the plasma and the first wall is not minimized. In a tokamak, the particles are confined by a magnetic field and as such, are kept away from the wall. A particle of charge q, mass m with a velocity $\mathbf{v}$ inside a magnetic field $\mathbf{B}$ feels the Lorentz force

$$\mathbf{F_L} = q \cdot (\mathbf{v} \times \mathbf{B}). \tag{2.1}$$

We can decompose the equation of motion in two, one for the velocity component parallel to the magnetic field and one for the component perpendicular to the magnetic field.

$$m\frac{d\mathbf{v}_\perp}{dt} = q \cdot (\mathbf{v}_\perp \times \mathbf{B}) \tag{2.2}$$

$$m\frac{d\mathbf{v}_\parallel}{dt} = 0 \tag{2.3}$$

When the magnetic field has a uniform distribution, the particle describes a circular motion in the perpendicular component while it moves with constant velocity in the parallel direction. The particles gyrate around the magnetic field lines with gyro-frequency ω and radius r_L (also called Larmor radius)

$$\omega = \frac{|q|B}{m} \qquad r_L = \frac{mv_\perp}{|q|B} \tag{2.4}$$

In this way, the motion can be divided in the motion of the guiding centre and the gyro-motion (see figure 2.1). The combination of these two motions results in a helical trajectory.
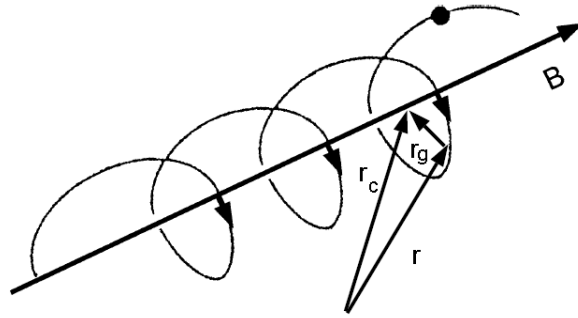
Figure 2.1: Typical trajectory of a charged particle inside a magnetic field. $\mathbf{r}_g$ is the Larmor radius in the Lorentz force direction and $\mathbf{r}_c$ is the vector position of the guiding centre.

2.1 Particle drifts

If the magnetic field is not uniform, as in a tokamak, particle drifts appear [1]. These drifts are caused by forces with non-zero component perpendicular to the magnetic field. The general expression of the drift velocity caused by a force $\mathbf{F}$ is

$$\mathbf{v} = \frac{1}{q}\frac{\mathbf{F} \times \mathbf{B}}{B^2}. \tag{2.5}$$

In a tokamak, the most important drifts are the $\mathbf{E} \times \mathbf{B}$-drift, the $\nabla\mathbf{B}$-drift and the curvature drift.

2.1.1 $\mathbf{E} \times \mathbf{B}$-drift

A particle with charge q moving in a electric field $\mathbf{E}$ feels a force $\mathbf{F} = q\mathbf{E}$. If the electric field is perpendicular to the magnetic field, the particle will feel the $\mathbf{E} \times \mathbf{B}$-drift

$$\mathbf{v_{E \times B}} = \frac{\mathbf{E} \times \mathbf{B}}{B^2}. \tag{2.6}$$

This drift does not depend on the charge or the mass of the particle, which means that electrons and ions will move in the same direction.

2.1.2 $\nabla\mathbf{B}$-drift

A gradient in the magnetic field causes the gyro-frequency and the Larmor radius to change during the trajectory. An additional force perpendicular to the magnetic field due to $\nabla\mathbf{B}$ acts on the particles. The expression of the $\nabla\mathbf{B}$-drift is the following

$$\mathbf{v_{\nabla B}} = -\frac{mv_\perp^2}{2qB^3}\nabla\mathbf{B} \times \mathbf{B} \tag{2.7}$$

where $v_\perp$ is the velocity perpendicular to the magnetic field. In this case, the direction and value of the drift is different for ions and electrons as the $\nabla\mathbf{B}$ drift depends on charge and mass of the particle.

2.1.3   Curvature drift

As the particles gyrate along the magnetic field lines, they follow curved field lines and therefore feel a centrifugal force. The expression of the curvature drift is

$$\mathbf{v}_{curv} = -\frac{mv_\parallel^2}{qB^3}\nabla\mathbf{B} \times \mathbf{B} \tag{2.8}$$

where $v_\parallel$ is the parallel velocity to the magnetic field. Similar to the $\nabla\mathbf{B}$-drift, the curvature drift depends on the sign of the charge and on the mass so that the direction and value of the drift are different for ions and electrons.

2.2   Particle orbits

As mentioned above, a charged particle moving in a magnetic field gyrates around a magnetic field line while the guiding centre moves with constant velocity. The drifts introduced in the previous section result in two types of guiding centre orbits if collisions are not taken into account [1]. Particles with a sufficient large velocity parallel to the magnetic field gyrate continuously around the torus. These are called the passing particles. Figure 2.2(a) shows an example of a passing particle orbit.

In a torus, the magnetic field is stronger in the inner region (high field side) than in the outer region (low field side) due to the $1/R$ dependence of the toroidal magnetic field. When a particle is moving to a higher magnetic field region, $v_\perp$ increases as a consequence of the conservation of the magnetic moment μ. Then, $v_\parallel$ decreases due to the conservation of the energy. At a certain point $v_\parallel = 0$ and the particle will be reflected to the outer region and gets trapped in a magnetic mirror, which is produced due to the force on the magnetic moment, $\mathbf{F} = \mu\nabla_\parallel\mathbf{B}$. This type of orbit is called banana because of its shape in a poloidal plane projection. An example of a trapped particle orbit is shown in figure 2.2(b). Figure 2.2 also shows the last closed flux surface, also called separatrix.

$$E = \frac{1}{2}mv^2 = \frac{1}{2}m(v_\perp^2 + v_\parallel^2) \quad ; \quad \mu = \frac{\frac{1}{2}mv_\perp^2}{B}. \tag{2.9}$$
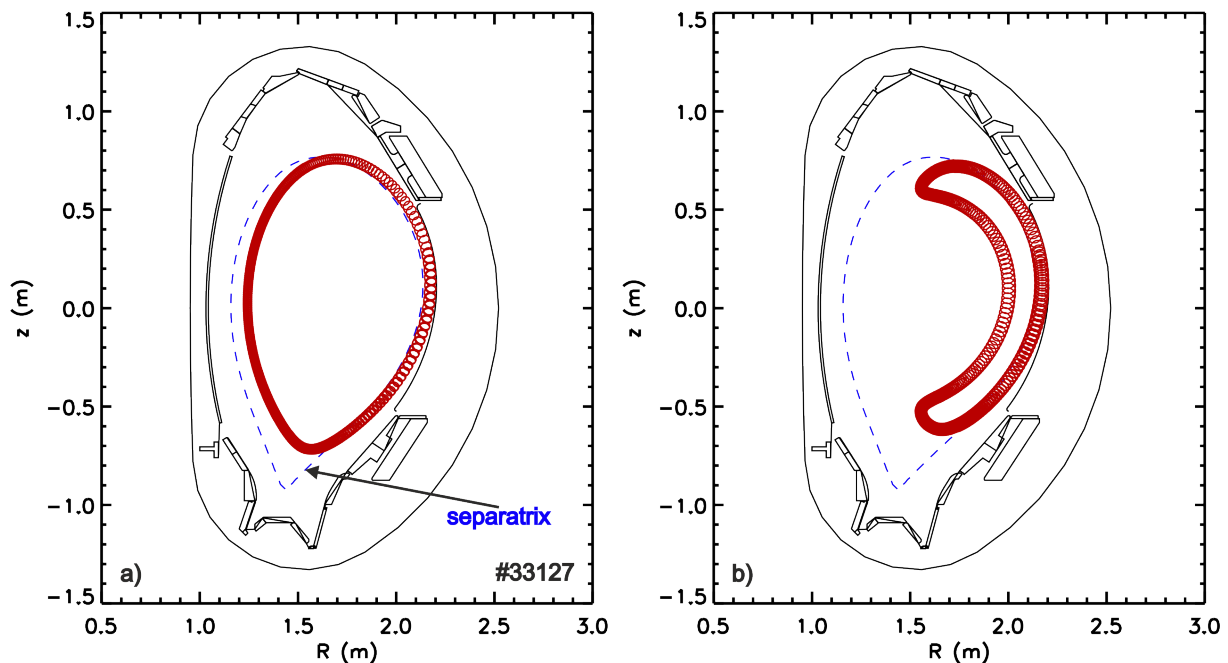
Figure 2.2: Poloidal plane projection of a passing orbit (a) and a banana orbit (b).

2.3 H-mode and Edge Transport Barrier

In divertor tokamaks, a high energy confinement regime is obtained when enough power is injected [3]. The high energy confinement regime, called H-mode, is characterised by an increase of density and temperature compared to the low energy confinement regime (L-mode). The transition from L-mode to H-mode results in an increase in plasma confinement by approximately a factor of 2. During the transition into H-mode, an edge transport barrier (ETB) evolves causing a reduced level of particle and heat transport perpendicular to the magnetic field. The ETB causes a steepening of the density and temperature gradients, and consequently pressure gradient at the plasma edge (see figure 2.3). The toroidal impurity velocity profile in H-mode discharges exhibits a very deep well close to the separatrix which can have negative values under certain conditions [4]. The profiles develop a pedestal structure within the ETB, which causes the improvement of the confinement in the H-mode as reflected in the increase of the stored energy shown in blue in figure 2.4(a). When the NBI is turned on, the stored energy, electron temperature and density increase and the plasma enters in the H-mode.
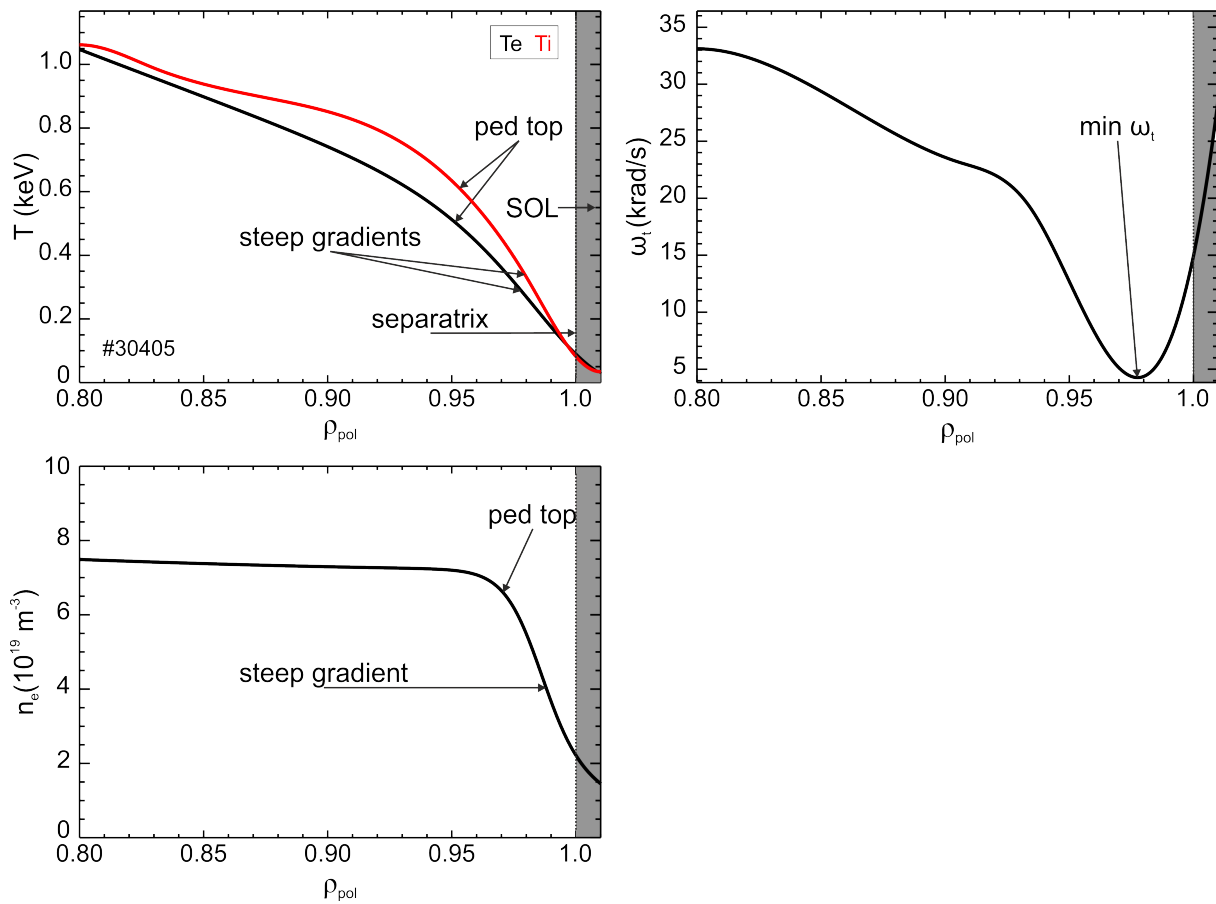
Figure 2.3: Typical profiles in H-mode discharges. The pedestal tops are the top of the pedestal structure. The scrape of layer (SOL), where the magnetic field lines are not closed, is represented in grey.
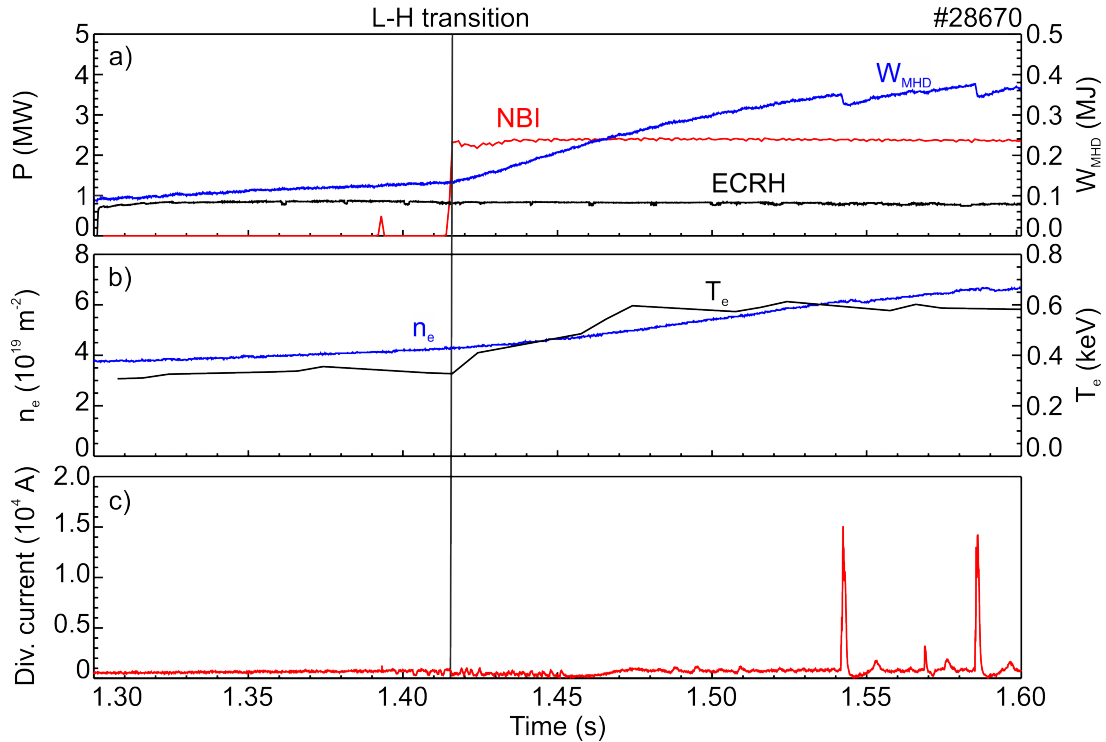
Figure 2.4: a) Time traces of ECRH power, NBI and plasma stored energy (W_{MHD}). b) Electron temperature and density. c) Thermo-currents in the divertor which is used as an ELM monitor.

2.4 Edge Localized Modes (ELMs)

The H-mode regime is accompanied by Edge Localized Modes, which are cyclic instabilities that expel particles and energy [5, 6]. ELMs have been observed in all tokamak devices when they are operating in H-mode. ELMs eject particles from the pedestal region, causing a degradation of the pedestal structure in density, temperature and pressure profiles. After an ELM, the profiles recover their steep gradients until the next ELM occurs. The physics triggering of an ELM is not well known yet, but it is believed that they are linked to the large gradients of the edge profiles. The most prominent candidate to explain the ELMs is the peeling-ballooning stability limit. The peeling stability limit implies a limit on the edge plasma current, while the ballooning stability limit results in a limit on the edge pressure gradient. Figure 2.5 shows a comparison between the temperature profiles before and after an ELM. The profiles experience a degradation as a consequence of the ELM.

The ELMs act also as a regulator of the impurities since these are also ejected during an ELM. The common way to detect an ELM is an increase of a thermo-current in the divertor due to the particles which are ejected. Figure 2.4 c) shows the the thermo-
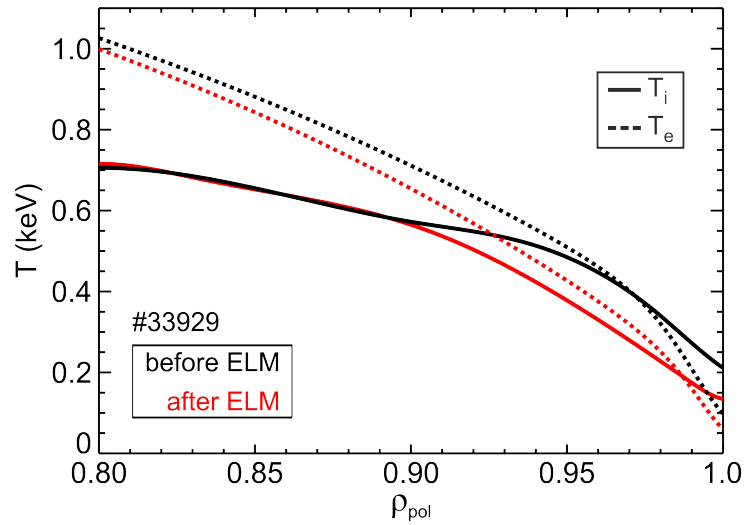
Figure 2.5: Comparison between temperature profiles before and after an ELM.

currents in the divertor. A spike in the signal indicates an ELM. There are two big ELMs around 1.54 s and 1.59 s. During these two ELMs, the stored energy decreases a little bit, due to the degradation of the pedestal.

For future fusion devices like ITER, it is very important to mitigate or suppress the ELMs to avoid damage of the machine, while maintaining the improved confinement of the H-mode.

Chapter 3

Diagnostics

High-resolution diagnostics are key to fusion research. The pedestal region is a very thin region (thinner than 2 cm on AUG) with large gradients that needs very high spatial and temporal resolution. In order to characterize properly the pedestal region, the time resolution has to be good enough to measure in-between two ELMs. In this section, the diagnostics that have been used during this thesis will be introduced (see figure 3.1).

3.1 Electron temperature and density measurements

In this work, the electron temperature (T_e) has been measured with the electron cyclotron emission (ECE) and Thomson scattering (TS) diagnostics. For the density (n_e), laser interferometry (DCN), impact excitation spectroscopy on a lithium beam (LIB) and Thomson scattering (TS) were used. The TS diagnostic gives information on electron temperature and density and thus, allows us to align both with respect to the separatrix position, as shown in section 3.3. A brief overview is introduced in the next sections.

Electron cyclotron emission (ECE)

The ECE diagnostic gives information on T_e. It measures the emission of electron radiation at its angular cyclotron frequency $\omega_{c,e} = eB/m_e$ and its harmonics $\omega_{k,e} = k\omega_{c,e}$. Assuming that the electron temperature is the radiation temperature and that electrons follow a Maxwellian distribution, the intensity at the cyclotron frequency follows Planck's law of
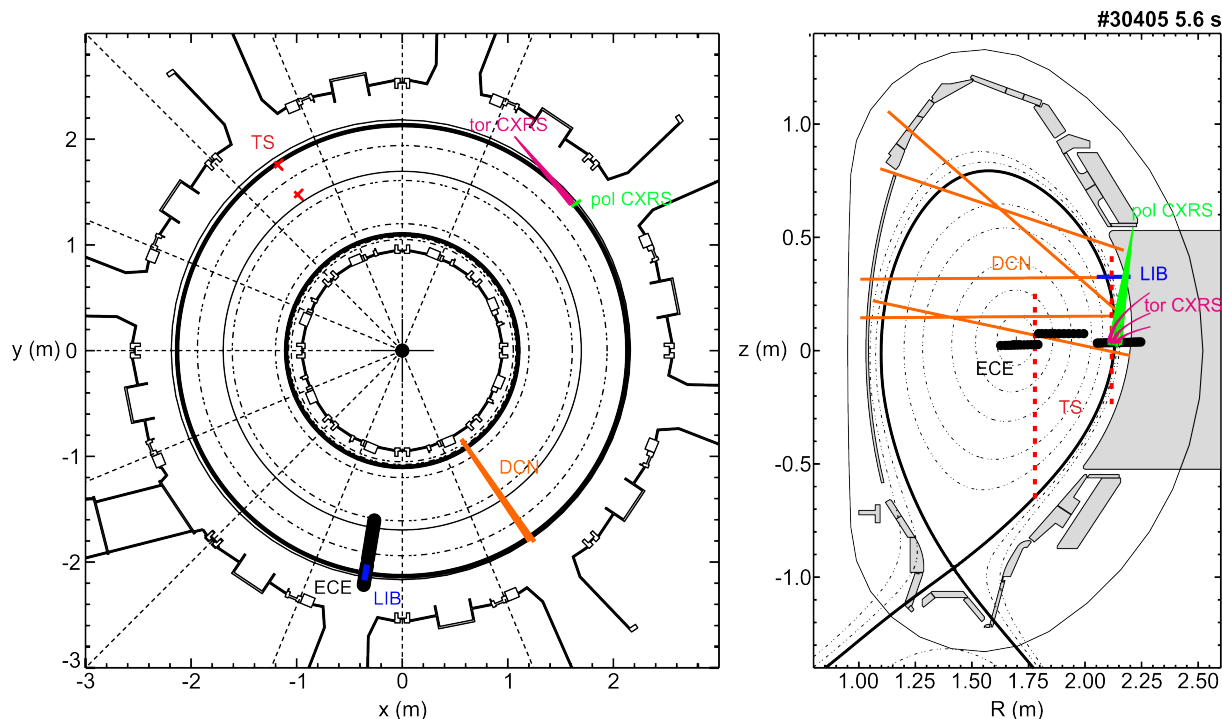
Figure 3.1: Toroidal (left) and poloidal (right) view of the diagnostics used during this thesis at AUG.

black-body radiation. At high temperatures, this results in the Rayleigh-Jeans expression

$$I_\omega = \frac{\omega^2}{2\pi^2 c^2} k_B T_e. \tag{3.1}$$

In a tokamak, the toroidal magnetic field, which is the dominant part of the total magnetic field, varies like $1/R$. This dependency allows us to associate the emission to a radial position. The assumption of black-body is only valid if the plasma is optically thick. If the plasma is not optically thick, as at the plasma edge due to the decrease in the density, the black-body law is not applicable. Due to this effect, the ECE measurements exhibit a peak close to the separatrix. Hence, in this region, the ECE data have not been used for fitting the electron temperature profile. At AUG, the ECE system has a spatial resolution of 1 cm and a temporal resolution of 1 µs [7, 8].

Thomson scattering (TS)

The Thomson scattering system measures the electron temperature (T_e) and density (n_e). The TS diagnostic is based on the elastic scattering of an electromagnetic wave by a charged particle. When an electromagnetic wave reaches the plasma, it accelerates the particles and the wave is scattered. The particles have velocities with respect to the initial

and scattered waves and, due to the Doppler effect, the frequency of the scattered wave is shifted. Due to the difference between electron and ion mass, mainly the electrons are accelerated. It is common to measure the scattered wave at 90°. The width of the scattered wave signal gives a measure of T_e. The intensity of the signal gives information about n_e. At AUG, there are two TS diagnostics, one viewing the plasma core and one the edge. The edge system has a spatial resolution of 3 mm and the core system has a resolution of 25 mm [9]. The TS diagnostic can measure every 8 ms. Due to its high resolution, the edge system is proper to characterize the pedestal region.

Impact excitation on a lithium beam

The lithium beam diagnostic injects high energy Li atoms in order to measure the density. When the Li atoms interact with the plasma, they are excited and emit radiation [10]. The profile of this radiation is correlated with the density. Due to several effects, the Li beam is attenuated when it penetrates the plasma. Hence, the Li beam diagnostic only gives information on the outermost region of the density profile. At AUG, the Li beam diagnostic has a spatial resolution of 5 mm and a temporal resolution of 50 µs [11].

DCN laser interferometry

The DCN diagnostic takes advantage of the interaction of the electrons with electromagnetic waves adding the dependence on the variation of the plasma refractive index N. A phase shift is obtained when comparing the propagation of an electromagnetic wave through the plasma with the propagation through the vacuum. This phase is directly correlated with the line-integrate density through the beam path. At AUG, this diagnostic has a temporal resolution of 300 µs [12].

3.2   Ion temperature and impurity rotation measurements

The most common technique to measure ion temperature and impurity rotation is charge exchange recombination spectroscopy (CXRS) [13]. The CXRS diagnostic measures the spectral lines emitted due to charge transfer from neutral to impurity ion species:

$$A^{Z+} + D \quad \rightarrow \quad A^{(Z-1)+^*} + D^+ \quad \rightarrow \quad A^{(Z-1)+} + h\nu + D^+. \qquad (3.2)$$
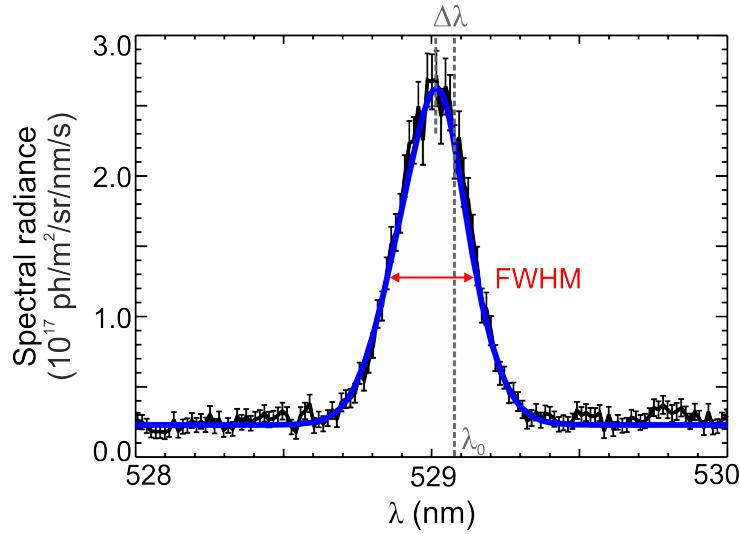
Figure 3.2: Typical spectrum measured with a CXRS diagnostic at AUG. The FWHM (Full Width at Half Maximum) is correlated to the temperature and the shift $\Delta\lambda$ is correlated to the toroidal impurity velocity. Figure taken from [14].

The neutrals are usually deuterium (D) or hydrogen (H) and are injected via neutral beam injection. The light emitted is analyzed with a spectrometer. Each species emits at a different wavelength and the measured spectrum gives information on its temperature and rotation. In particular, the temperature is derived from the width of the signal and velocity is derived from the Doppler shift (see figure 3.2).

The lines of sight (LOS) of the CXRS system are the viewing lines of the plasma where the diagnostic is pointing at. The active line comes from the points where the LOS intercept the neutral beam. The passive lines are emitted at the plasma edge, due to charge exchange with thermal neutral deuterium and electron impact excitation [15].

The impurities that are usually measured at AUG are boron (B) and nitrogen (N) but in helium (He) plasmas the main ion can be measured. Usually low Z impurities are measured because they are fully ionized, while high Z impurities have a smaller concentration in the plasma and they are not fully ionized throughout the whole plasma.

Figure 3.2 shows the spectral radiance obtained with one of the edge CXRS systems at AUG [16, 17]. The full width at half maximum (FWHM) of the spectral radiance is directly correlated with the temperature of the measured species:

$$T = \frac{mc^2}{8ln(2)\lambda_0^2 e^2} FWHM^2 \tag{3.3}$$

where m is the mass of the measured species, c is the speed of light, λ_0 is the theoretical wavelength of emission and e is the electron charge. The shift due to Doppler effect

provides the rotation velocity $\mathbf{v}_t$ of the considered species

$$\frac{\Delta\lambda}{\lambda} = \frac{\mathbf{v}_t \cdot \mathbf{e}_{LOS}}{c} \tag{3.4}$$

where $\mathbf{e}_{LOS}$ is the unit vector along the LOS. Note that $\mathbf{v}_t = \omega_t \times \mathbf{R}$.

In this thesis, two CXRS systems at AUG have been used to characterise the edge profiles [16, 17]: the toroidal edge CXRS system, which has a spatial resolution of 1-3 mm, and the poloidal edge CXRS system, which has a spatial resolution of 3-5 mm in the steep gradient region. Both CXRS systems have a standard temporal resolution of 2.3 ms but it can be turned down to 50 μs [17].

3.3   Profile alignment

The different profiles are obtained by combining the data of various diagnostics. The magnetic equilibrium is assumed to be toroidally symmetric. As the diagnostics measure at different toroidal and poloidal positions, small uncertainties in the radial position can arise when mapping the profiles onto the magnetic equilibrium. Thus, the measured profiles of the different diagnostics have to be aligned in order to reduce uncertainties in the radial position. This adjustment is very important in the ETB region which has a spatial extent of only 1.5-2 cm at AUG. The steep gradients in the ETB allow to reduce the uncertainties down to 2-3 mm [18].

Power balance and parallel heat transport studies based on a 1D heat conduction model [19, 20] determine that electron temperature at the separatrix has to be approximately 100 eV in H-mode discharges of AUG. The procedure to align the profiles is the following: first, the T_e profile from TS is shifted to obtain 100 eV at the separatrix. Then, the T_e profile measured with ECE is shifted to match the profile measured with TS. As mentioned above, TS gives information on T_e and n_e. The shift used for the TS T_e profile is applied to the TS n_e profile. After that, the lithium beam n_e profile is shifted to match the TS n_e profile. Thus, the T_e profile and n_e profile are aligned. The T_i profile, measured with the CXRS systems, is aligned by shifting T_i such that the position of the steepest gradients matches the one of T_e. This assumption is valid for high collisionality discharges as at high collisionality the ions and electrons are well coupled [21]. The uncertainty in the alignment between T_e and T_i is less than 5 mm. The toroidal impurity velocity (ω_t) profile is intrinsically aligned to the T_i profile because they are measured with the same diagnostic. Figure 3.3 shows an example of the experimental data before and after the alignment.
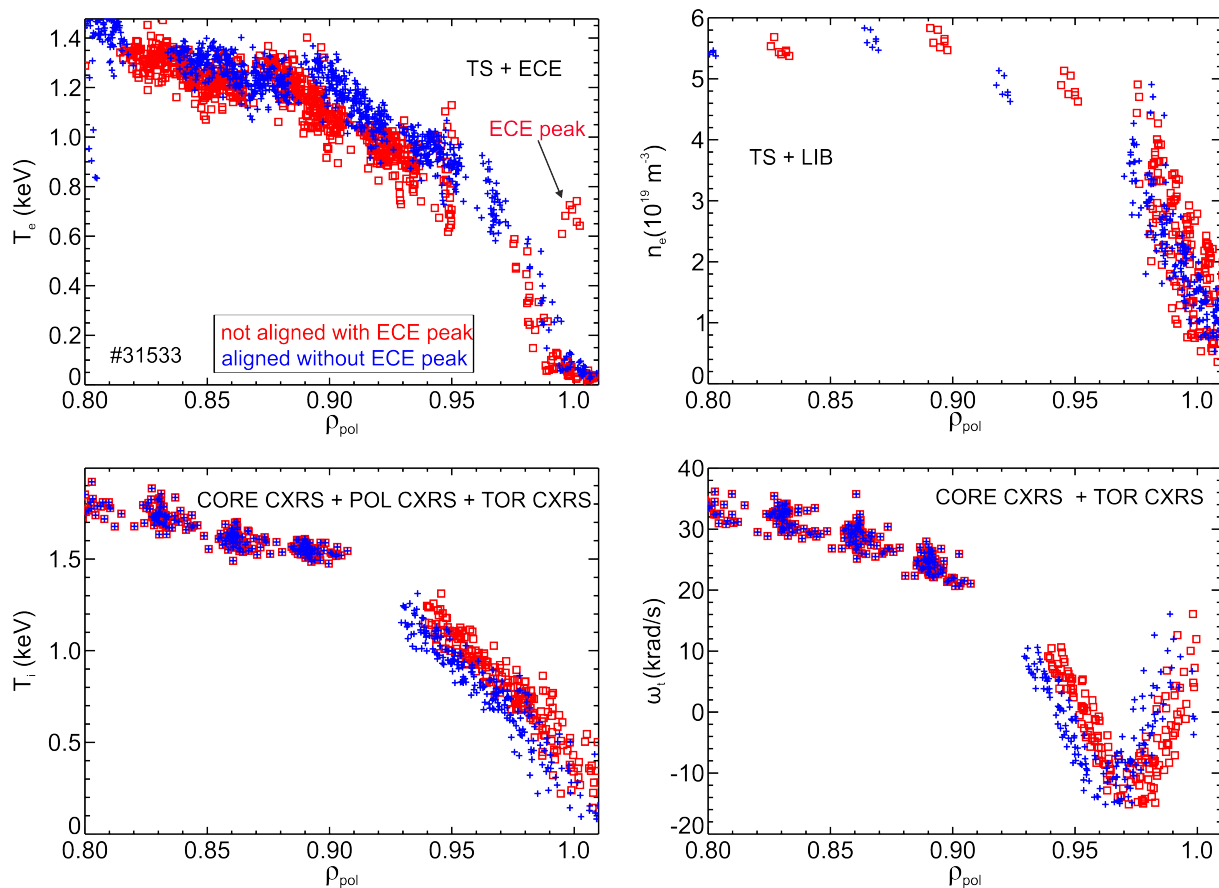
Figure 3.3: Example of aligned (blue) and no aligned (red) experimental data.
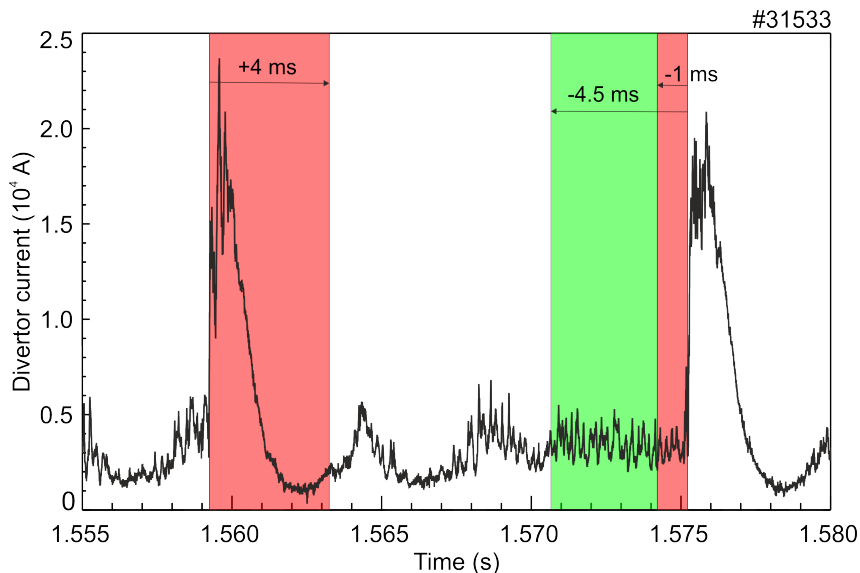

Figure 3.4: Schematic of the ELM synchronization technique using the divertor current to identify ELMs. The data highlighted in red are excluded. Pre-ELM profiles are taken from the measurements obtained in the time window highlighted in green.

3.4   ELM synchronization

As described in section 2.3, ELMs produce a collapse of the pedestal region in temperature and density. A characterization of the H-mode pedestal requires to remove the effects from the ELM. The ELM synchronization technique allows us to sort the measured data with respect to the ELM onset [22]. This allows us to study time windows which are not affected the ELM, as shown in figure 3.4. This can be done because the ELMs are cyclic. In this thesis, in general, useful data are considered 4 ms after the start of an ELM and from 4.5 ms to 1 ms before the following ELM. These conditions imply that, between two ELMs, a 3.5 ms time window is used to obtain valid data. Note that depending on the discharge the time that spans from 4 ms after the start of an ELM to 4.5ms before an ELM can be 0. In some discharges the parameters of the ELM synchronization had to be slightly modified due to high ELM frequency.

Chapter 4

Database

The aim of this thesis is to progress in the understanding of the pedestal. Recently, AUG has reached low collisionality plasmas with the tungsten wall. The concept of collisionality will be explained in section 4.2. This thesis is focused on the study of the ion temperature pedestal in high and low collisionality plasmas. A correlation between toroidal impurity velocity, ion temperature, electron temperature and density is studied.

To carry out this study, a database has been compiled. The database allows us to study correlations between a large number of parameters. The database has 46 discharges from AUG and, for each discharge, one or several time windows have been analyzed. In total, the database consists of 89 time windows. For each time window, the profiles are aligned and fitted and several parameters of the plasma are obtained. The difference between this study and other similar studies is that in this database, the toroidal impurity velocity profile is included. It will be shown that the minimum in the toroidal impurity velocity profile is strongly correlated with the collisionality.

In section 4.1, the procedure to obtain the profiles as well as the importance of the selected fitting procedure will be explained. The parameters that have been studied will be introduced in section 4.2.

4.1   Pedestal characterization

As introduced in section 3.3, in order to obtain the profiles, a radial profile alignment has to be performed. Once the profiles are aligned, a fitting procedure is applied to get a continuous profile. All the profile characteristics are obtained from the fit, not from the experimental data directly.
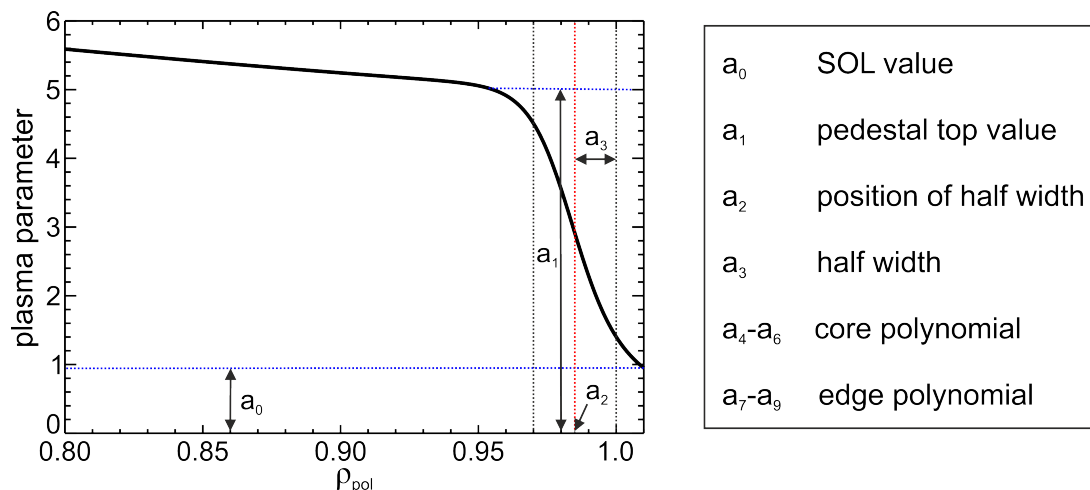
Figure 4.1: Schematic and explanation of mtanh coefficients.

The pedestal region can be characterised by its pedestal top value, the gradient and the width of the steep gradient region. Hence, the fit has to be smooth enough in the pedestal region to get a good characterisation. In this thesis, two fitting procedures have been used: modified hyperbolic tangent function and a spline fit. In the following sections, both methods will be introduced.

4.1.1 Modified hyperbolic tangent function (mtanh method)

The mtanh function allow us to fit a smooth function through the whole profile (core, pedestal and SOL). The mtanh function is a modified hyperbolic tangent [22]. The modification of the hyperbolic tangent are polynomials that are added to fit the core and SOL regions:

$$f_{mtanh}(x) = \frac{a_0 + a_1}{2} + \frac{a_1 - a_0}{2} \cdot \frac{(1 + a_4 z + a_5 z^2 + a_6 z^3)e^z - (1 + a_7 z + a_8 z^2 + a_9 z^3)e^{-z}}{e^z + e^{-z}}$$

(4.1)

where $z = (a_2 - x)/a_3$. The meaning of the coefficients a_n are shown in figure 4.1.

The order of the polynomials is varied to get the best possible fit. In this thesis, the mtanh function is used to fit the T_e and n_e profiles due to the strong pedestal shape of these profiles. Note that the mtanh fit imposes a pedestal shape and, in some cases, the T_i and ω_t profiles are not well described by mtanh fit. An example of n_e and T_e profiles fitted with mtanh function is shown in figure 4.2.
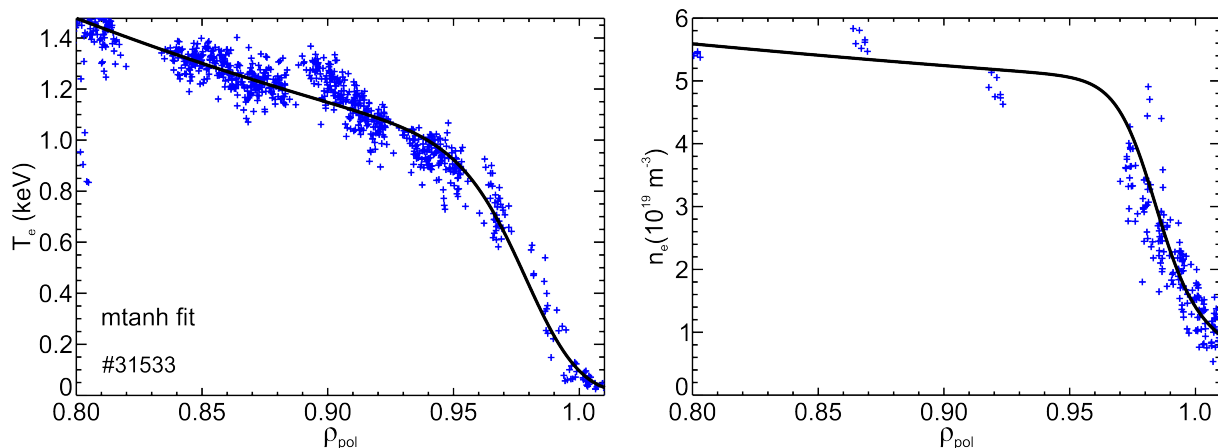
Figure 4.2: Example of mtanh fit of T_e (left) and n_e (right).

4.1.2   Spline method

The spline method uses a function defined piecewise by polynomials. In this case, the polynomials are of order three. A general expression of a spline function could be the following

$$F(x) = \begin{cases} a_0 + a_1 x + a_2 x^2 + a_3 x^3 & x_1 \leq x < x_2 \\ b_0 + b_1 x + b_2 x^2 + b_3 x^3 & x_2 \leq x < x_3 \\ c_0 + c_1 x + c_2 x^2 + c_3 x^3 & x_3 \leq x \leq x_4. \end{cases} \tag{4.2}$$

An important condition of $F(x)$ is that it has to be continuous. The number of polynomials used in this thesis in the spline function are three or four. For each fit, three or four polynomials function are used depending on the resulting fit to the data. The spline function has been used to fit T_i and ω_t profiles because these profiles have a smoother shape than the T_e and n_e profiles. Unlike the mtanh fit, the spline fit does not give the pedestal parameters directly by its coefficients. An example of a spline fit is shown in figure 4.3.

4.2   Database parameters

In this section, the relevant parameters of the database are introduced. Once the profiles are fitted, several parameters are derived from them: the pedestal top value, pedestal top position, pedestal width, steepest gradient position and steepest gradient value. One way to determine the pedestal top position is by calculating the second derivative of the pedestal profile as shown in figure 4.4. The position of the pedestal top can be estimated
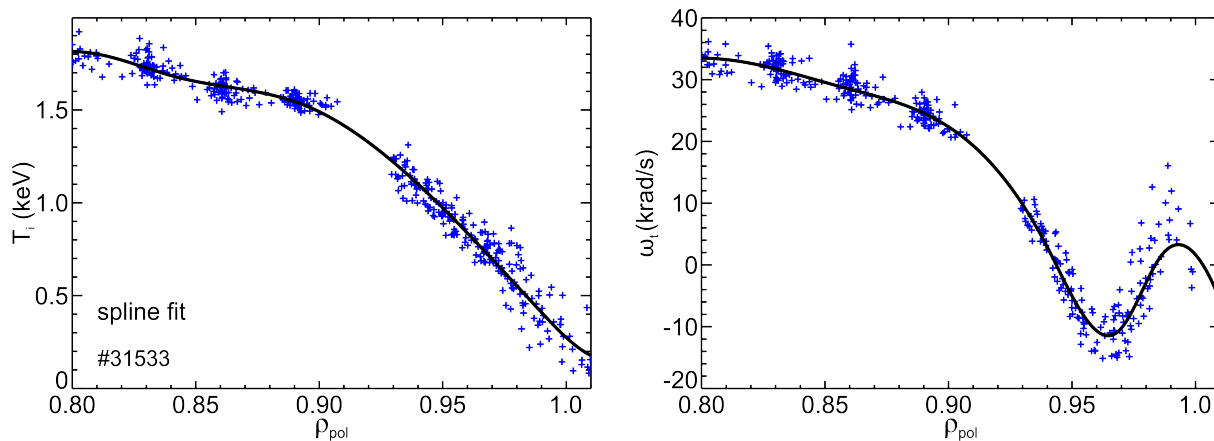
Figure 4.3: Example of spline fit: T_i (left), ω_t (right).
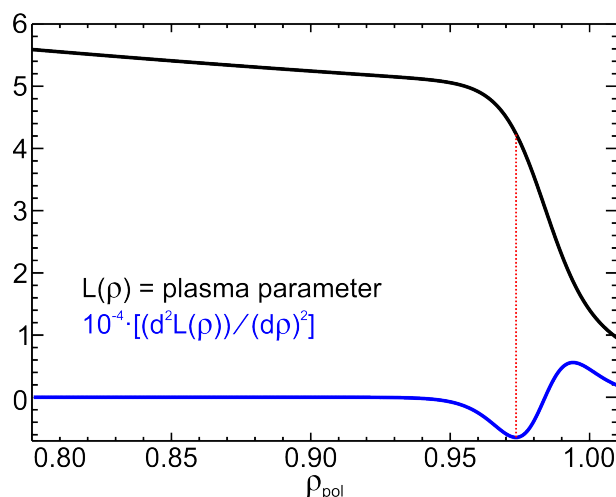
Figure 4.4: Representation of a plasma parameter $L(\rho)$ and its second derivative. The position of the pedestal top is located in the minimum of its second derivative.

as the position of the minimum of the second derivative. The minimum in the toroidal impurity velocity is well determined as shown in the ω_t profile of figure 4.3.

An important parameter is the safety factor q. It represents the number of required toroidal turns to complete a poloidal turn. The safety factor plays an important role in the plasma equilibrium.

With the safety factor and the profiles, the collisionality can be calculated. The collisionality is a dimensionless quantity which represents how important the collisions are. The collisionality is the number of collisions that a particle experiences on a banana orbit. The theoretical expression of the collisionality is
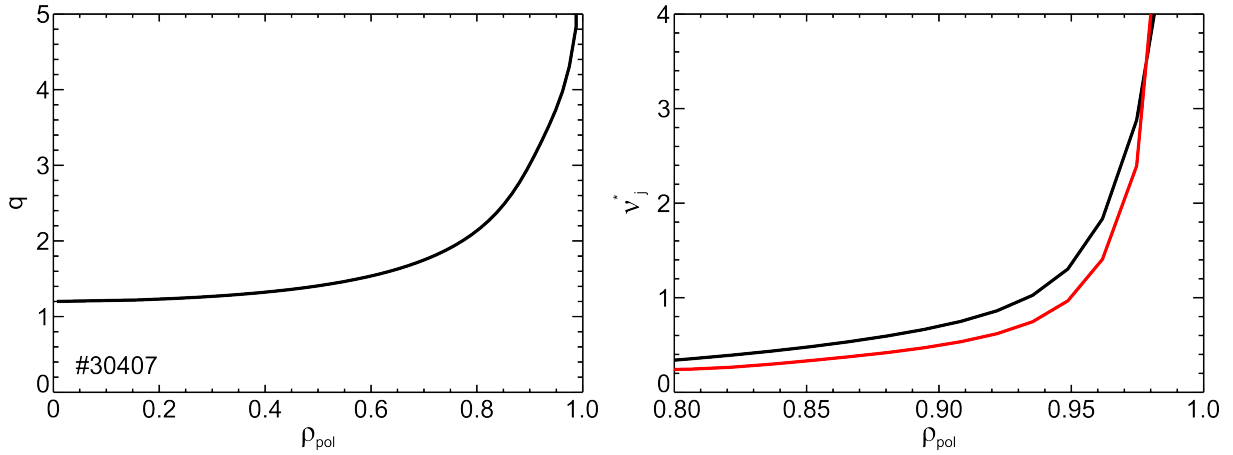
$$\nu_j^* = \frac{\nu_j}{\omega_{bj}} \tag{4.3}$$

Figure 4.5: Typical safety factor (left) and collisionality (right) profiles.

where $j = i$, e, stands for electrons or ions, ν_j is the collision frequency and ω_{bj} is the bounce frequency. The expressions used to calculate the electron and ion collisionality [23] are the following

$$\nu_e^* = 0.0012 \cdot \frac{qR_0^{3/2}Z_{eff}n_e[10^{19}m^{-3}]}{r^{1/2}\epsilon(T_e[keV])^2} \tag{4.4}$$

$$\nu_i^* = 4.9 \cdot 10^{-5} \cdot \frac{qR_0^{3/2}Z_{eff}^4(17.3 - \frac{1}{2}ln(n_i[10^{20}m^{-3}]) + \frac{3}{2}ln(T_i[keV]))n_i[10^{19}m^{-3}]}{r^{1/2}\epsilon(T_i[keV])^2} \tag{4.5}$$

where q is the safety factor, R_0 is the major radius, Z_{eff} is the effective charge state , r is the radial coordinate and ϵ is the ratio between the minor and the major radius $\epsilon = a/R_0$. Figure 4.5 shows a typical q profile and collisionality profile. Note that the safety factor and collisionality go to infinite at the separatrix.

The characteristics of a plasma depends on the elements of which it is composed. The database includes deuterium, hydrogen and helium discharges. In some discharges, impurity seeding, usually nitrogen, is applied. When applying impurity seeding it has been observed differences in the location of the density pedestal top [24]. The amount of gas introduced in the plasma per unit of time is the fuelling. The triangularity δ and the elongation κ are parameters that describe the shape of the plasma. Both parameters refer to the separatrix poloidal cross section shape. The elongation is bigger when the shape looks more thinner (see black shape in figure 4.6a) and the triangularity is bigger when the shape looks more like a triangle (see black shape in figure 4.6b).

Table 4.1 shows the range the parameters included in the database. P_{heat} is the heating power, f_{ELM} is the ELM frequency, I_p is the plasma current and B_t is the toroidal magnetic field.
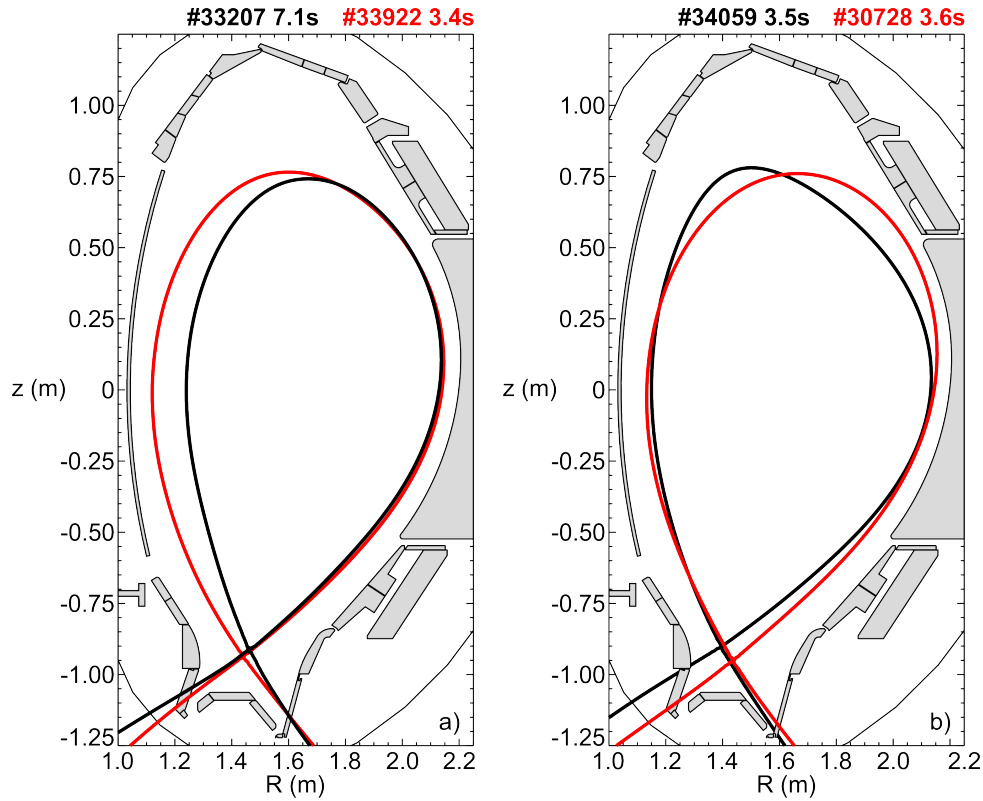
Figure 4.6: a) Separatrix of a high (low) elongation discharge in black (red). b) Separatrix of a high (low) triangularity discharge in black (red).

Parameter	Range
P_{heat}	3.5 - 15.4 [MW]
f_{ELM}	32.4 - 201.7 [Hz]
I_p	0.62 - 1.14 [MA]
B_t	1.97 - 2.5 [T]
δ	0.18 - 0.40
κ	1.59 - 1.74
$\nu_e^*(\rho = 0.97)$	0.62 - 4.20
$\nu_i^*(\rho = 0.97)$	0.24 - 3.15
$D_{fuelling}$	0 - 2.81 [10^{22} part/s]
$H_{fuelling}$	0 - 2.56 [10^{22} part/s]
$N_{fuelling}$	0 - 2.47 [10^{22} part/s]

Table 4.1: Range of the parameters included in the database.

Chapter 5

Results

The pedestal is a very important region to understand the behaviour of the plasma. The impact of the collisionality on the profiles as well as understanding the relation of the position (value) of the different pedestals with the position (value) of the minimum in the toroidal impurity velocity could help to progress in pedestal physics. This section shows the results obtained during this thesis.

5.1 Comparison between profiles at low and high ν^*

This section will show the main differences between profiles at high and low collisionality. Figure 5.1 shows time traces of discharge #33207. In this discharge, four times windows were analyzed. From the first time window (black) to the second one (red) the NBI power is increased. The toroidal impurity velocity increases in the core but decreases in the edge. Furthermore, the density decreases and ion and electron temperature increase. Comparing the second (red), third (blue) and fourth (green) time windows, the NBI power is constant but the deuterium fuelling decreases. The toroidal impurity velocity in the core keeps constant but it decreases at the edge. Again, density decreases and ion and electron temperature increase. Expressions 4.4 and 4.5 show that the collisionality decreases when the density decreases and when the temperature increases, while keeping the safety factor constant. This behaviour is observed in the temporal evolution of the selected time windows in this discharge. Thus, the collisionality in this discharge is decreasing in all analyzed time windows. Specifically, the ion collisionality at $\rho_{pol} = 0.97$ goes from 1.31 to 0.24. Figure 5.2 compares the profiles in the first time window (highest collisionality) with the profiles in the fourth time window (lowest collisionality). As mentioned above,
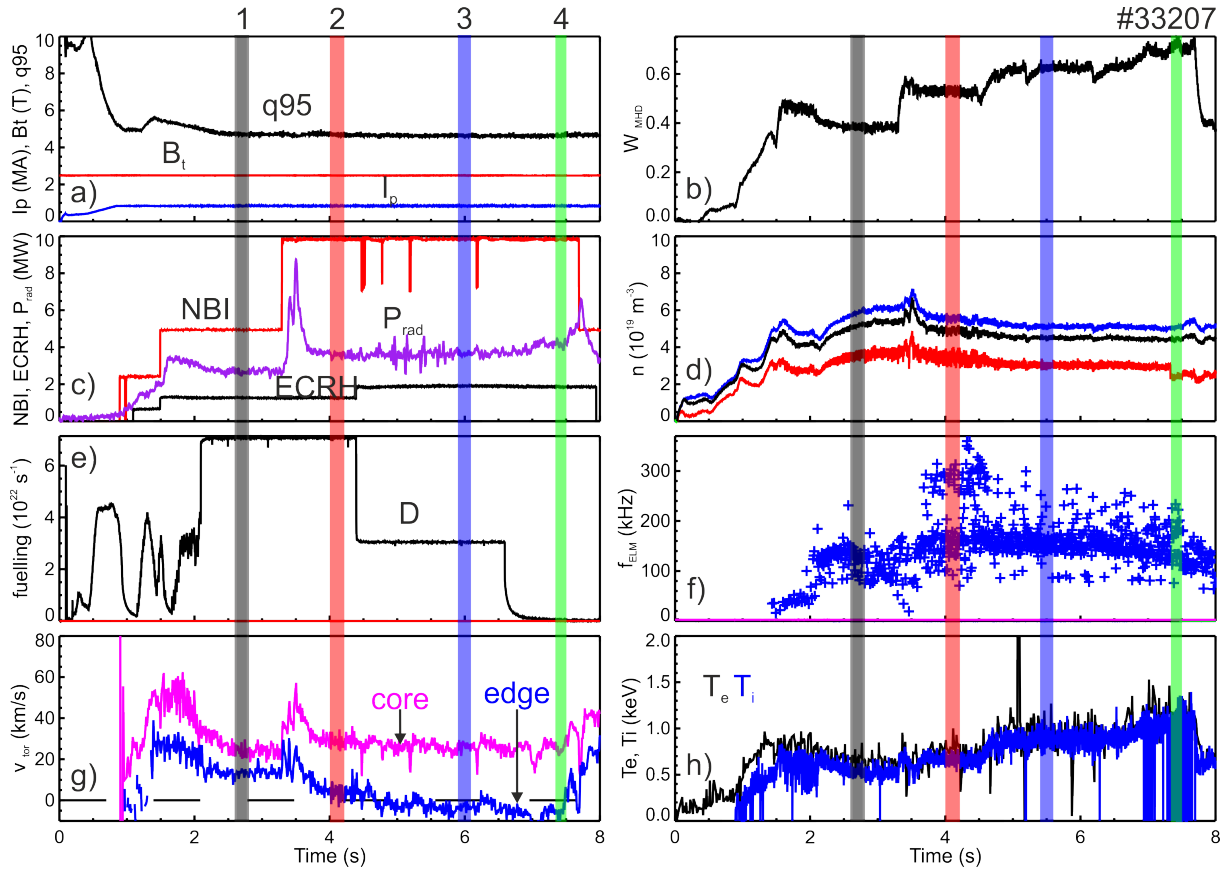
Figure 5.1: Time traces: a) plasma current, toroidal magnetic field and safety factor at the flux surface containing 95% of the total poloidal flux inside the separatrix, b) plasma stored energy, c) NBI, ECRH and radiation power, d) density, e) fuelling, f) ELM frequency, g) toroidal velocity, h) electron and ion temperature of discharge #33207. Analyzed times windows are highlighted in colours.

the temperature is higher in the low collisionality case and the density is higher in the high collisionality case. Furthermore, the ion temperature is larger than the electron temperature at low collisionality. At high collisionality, the ion and electron temperature are coupled and at low collisionality they are decoupled. The minimum in the toroidal velocity is negative in the low collisionality case and positive in the high collisionality case [25].

5.2 Dependency of ω_t^{min} on ν^*

This section describes the correlations between the minimum in the toroidal impurity velocity profile with the collisionality. The relation between the values of T_i, T_e and n_e at the pedestal top with the value of the minimum in the toroidal impurity rotation profile
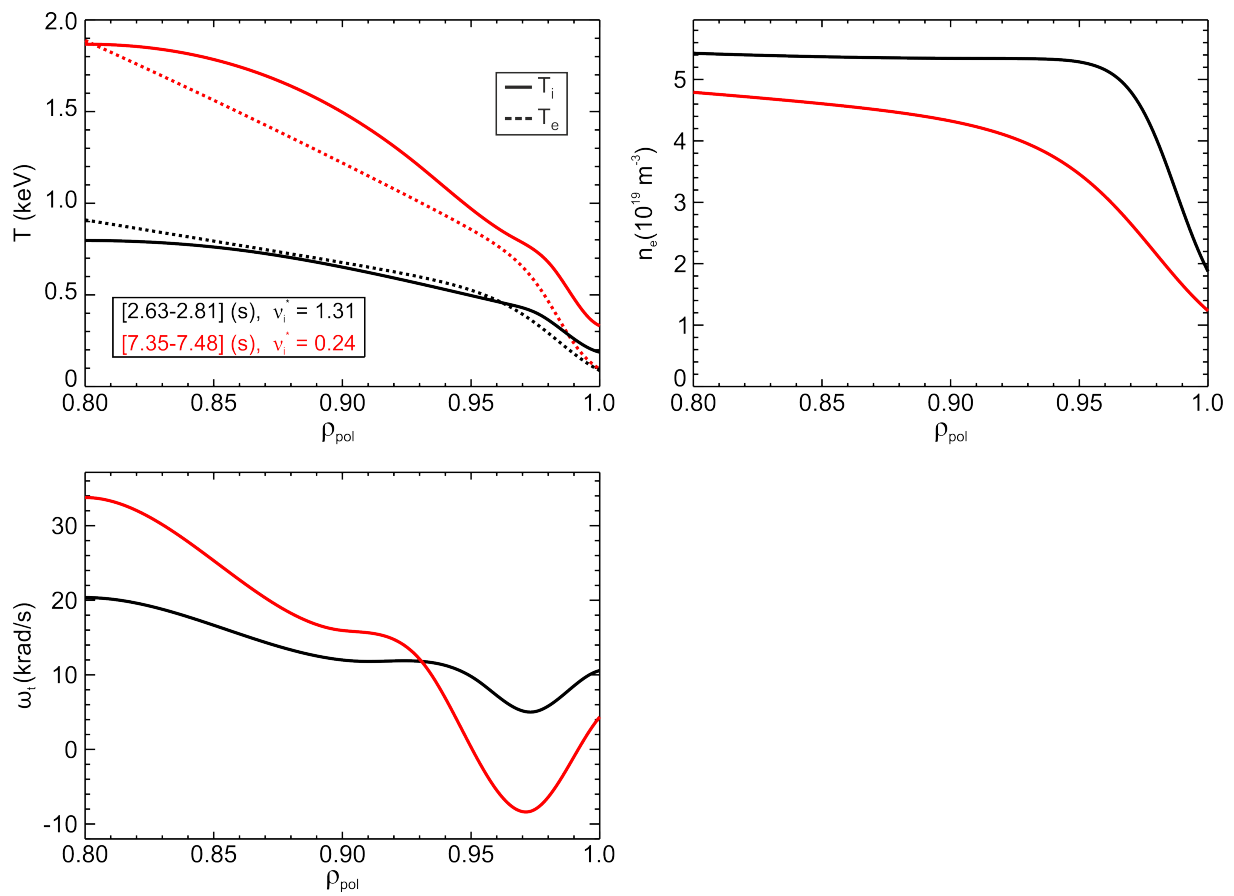
Figure 5.2: Comparison between profiles of discharge #33207 at low collisionality (red) and high collisionality (black).
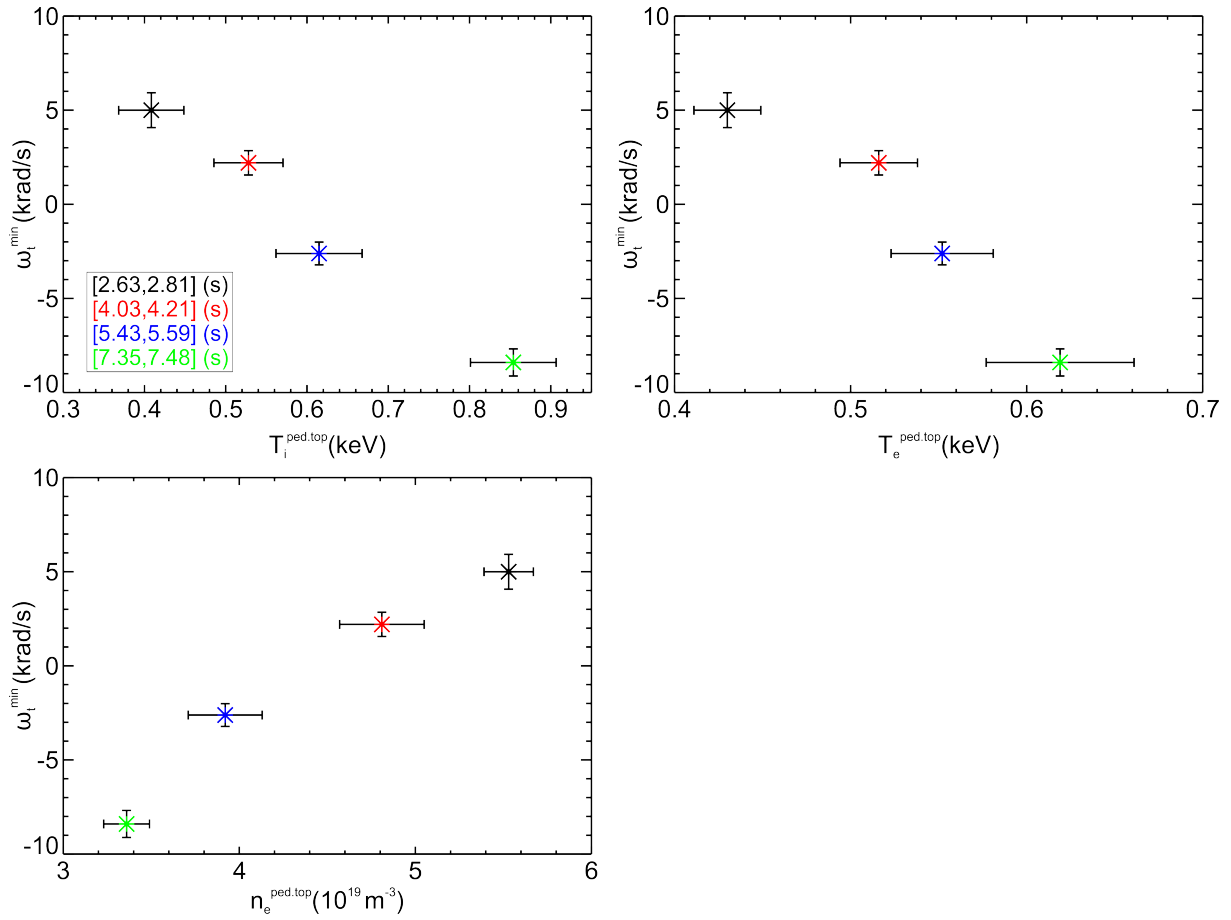
Figure 5.3: Correlations between the values of $T_i^{ped.top}$, $T_e^{ped.top}$, $n_e^{ped.top}$ and ω_t^{min} in the four time windows selected of the discharge #33207.

for the four time windows considered in discharge #33207 is represented in figure 5.3. When the density decreases and the temperature increases, i.e collisionality decreases, the value of the minimum in ω_t decreases reaching negative values. As mentioned in the previous section, the minimum in the toroidal impurity velocity changes sign when collisionality is low enough. Negative values of the toroidal impurity velocity means that the particles are moving in the counter-current direction and in opposite direction of the plasma core.

Figure 5.3 will be reproduced in figure 5.4 including all the time windows of the database. The trend is the same in both figures. When the temperature increases enough (or the density is low enough), the minimum in the toroidal impurity velocity becomes negative as the collisionality is decreasing. In figure 5.4, a linear fit is included for deuterium discharges (black) and for deuterium with nitrogen seeding discharges (blue). The fits of the temperature data without nitrogen seeding are slightly steeper than the fits to the
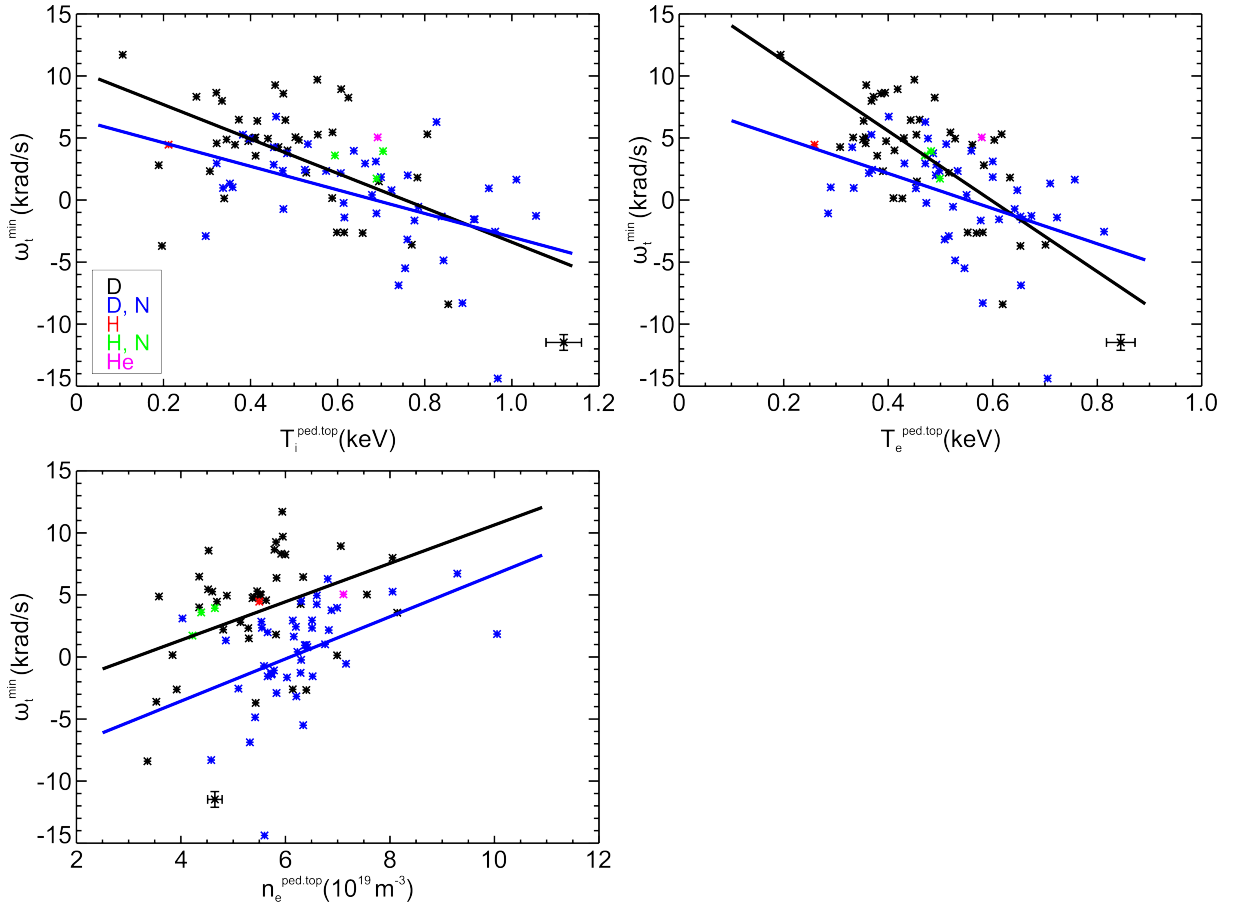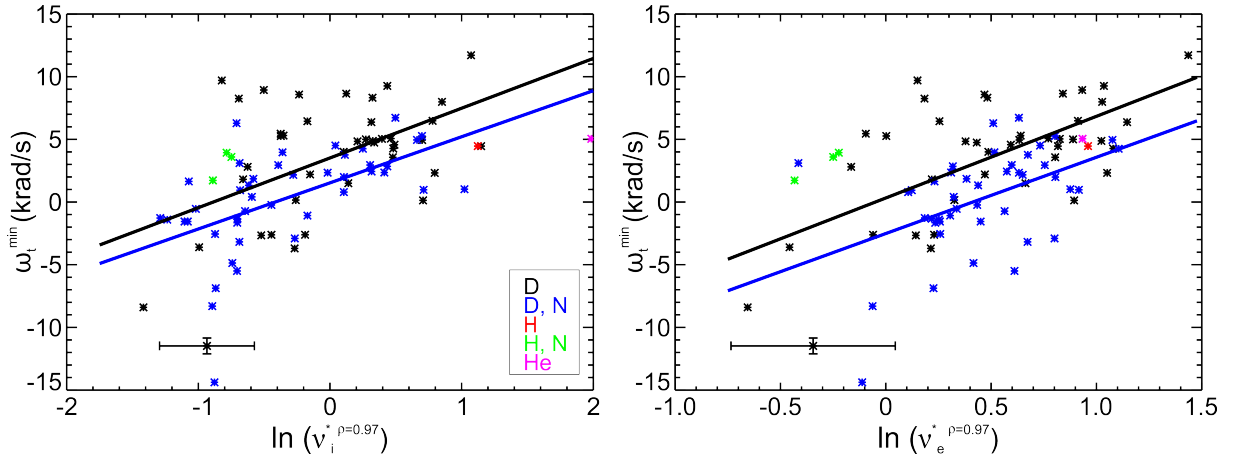
Figure 5.4: Correlations between the values of $T_i^{ped.top}$, $T_e^{ped.top}$, $n_e^{ped.top}$ and ω_t^{min} for all the database.

data with seeding. The fit to the density data without nitrogen seeding has an offset of around 5 krad/s with respect to the fit to the data with nitrogen seeding.

To confirm the dependency of the minimum in ω_t on the collisionality, both quantities are represented in figure 5.5. The collisionality is taken at $\rho = 0.97$. When the collisionality is low enough, the minimum in ω_t reaches negative values, while for high values of the collisionality, the minimum in ω_t is positive. The uncertainties in the collisionality shown in figure 5.5 are calculated via Gaussian error propagation using uncertainties of temperature and density. Uncertainties in the major radius, safety factor and Z_{eff} have not been taken into account. Error bars are only included for one data point on each graph for clarity. This database shows a robust dependence of ω_t on ν^* including changes in shape, plasma current, fuelling, ELM frequency and toroidal magnetic field.

Figure 5.5: Correlations between collisionality and ω_t^{min}.

5.3 Correlations between positions of pedestal top and ω_t^{min}

The objective of this section is to identify correlations between the position of the pedestals and the minimum in the toroidal impurity velocity. Figure 5.6 shows the position of ω_t^{min} versus the position of $n_e^{ped.top}$ and $T_i^{ped.top}$ for the whole database.

Including all points of the database, no correlation between position of the ω_t^{min} and the position of $n_e^{ped.top}$ is observed. However, when limiting the parameter space to $\nu_i^* > 0.9$ (high collisionality), $0.20 < \delta > 0.26$, $I_p > 1\ MA$ and $5\ MW < P_{heat} < 16\ MW$, shows a clear trend between the radial position of ω_t^{min} and $n_e^{ped.top}$ and $T_i^{ped.top}$. Figure 5.7 shows that the radial position of ω_t^{min} is located at $n_e^{ped.top}$ and ω_t^{min} moves outwards when $T_i^{ped.top}$ and $n_e^{ped.top}$ move outwards.

This dependence is also studied at low collisionality. The results for low collisionality are shown in figure 5.8. In this case, there is no correlation between the position of ω_t^{min} and the position of $n_e^{ped.top}$, but there is a correlation between the position of ω_t^{min} and the position of $T_i^{ped.top}$. This suggest that the physics mechanism setting the pedestal may be different at low and high collisionality. Note, however, that the uncertainties of the radial profile alignment are larger at low collisionality as the electrons and ions are more decoupled and, hence, the assumption of $\rho(\nabla T_i) = \rho(\nabla T_e)$ may not be valid.

The trends observed in figures 5.7 and 5.8 are clear, but it is important to mention that the data included in the figures have uncertainties. The positions derived from T_e and n_e profiles have a uncertainty of 5 mm due to the spatial resolution of the diagnostics, that corresponds to 0.01 in ρ at AUG. On the other hand, the positions derived from T_i and
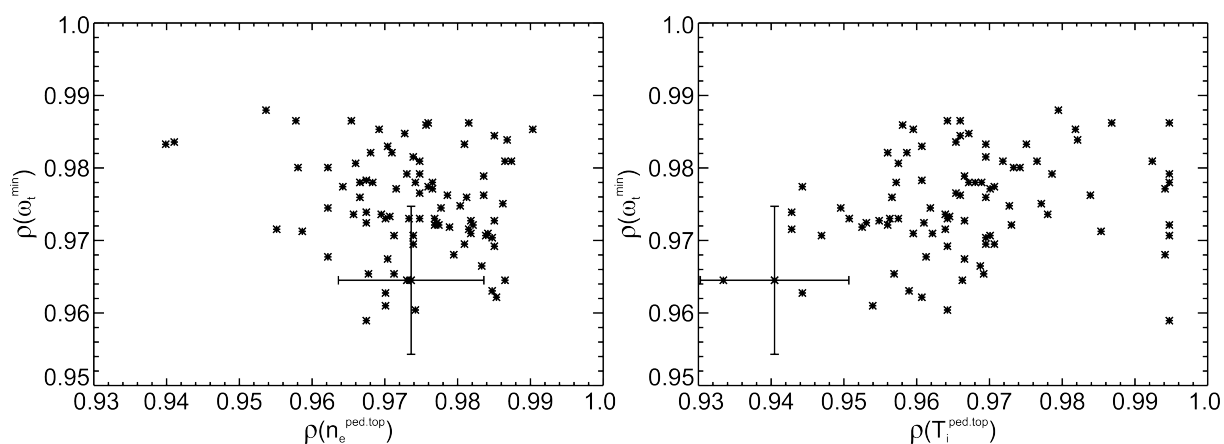
Figure 5.6: Correlations between position of the minimum in the toroidal impurity velocity and position of n_e pedestal top (left) and position of T_i pedestal top (right).
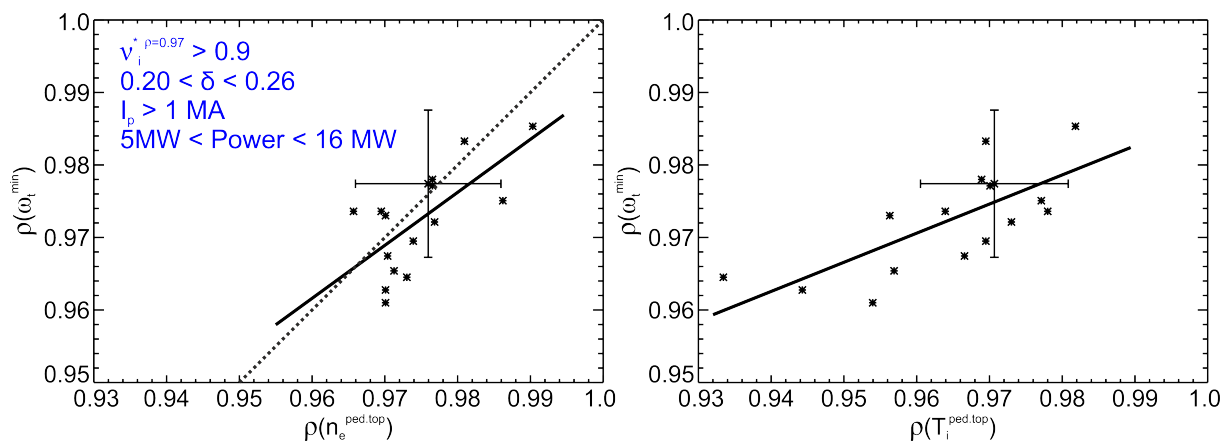

Figure 5.7: Repetition of figure 5.6 for only high collisionality discharges. The dash line is the identical line $y = x$.
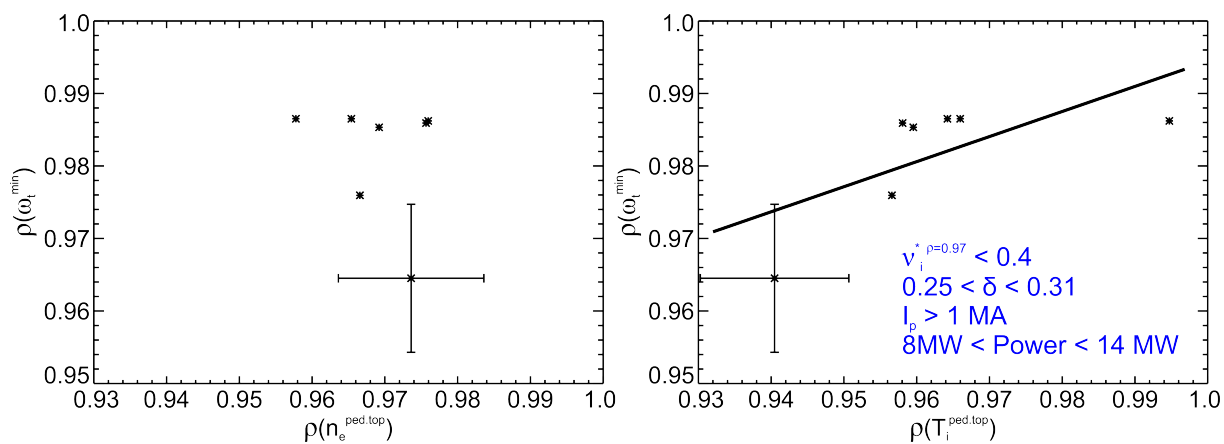

Figure 5.8: Repetition of figure 5.6 for only low collisionality discharges.

ω_t profiles have two sources of uncertainties: the spatial resolution of the diagnostics and the uncertainties due to the radial profile alignment.

Chapter 6

Summary and conclusions

This thesis contributes to the characterization of the pedestal at high and low collisionality. The pedestal is a very thin region characterized by steep gradients and is developed when the plasma enters in the high confinement mode (H-mode).

A database based on measurements from the ASDEX Upgrade tokamak was set up in order to find correlation between various plasma parameters. This thesis compares the behaviour of the ion and electron pedestal and the minimum in the toroidal impurity velocity, ω_t, at low and high collisionality. Section 5.1 shows that the ion temperature is larger than electron temperature at low collisionality, while they are similar at high collisionality as in this regime the ion and electron channels are well coupled. At low collisionality, the minimum in ω_t is negative, in counter-current direction and in opposite direction to the plasma core. At high collisionality, the minimum in ω_t is positive. This behaviour has been observed for the full database.

In high collisionality discharges, the position of the minimum in ω_t is located at the position of the density pedestal top. Moreover, the position of the minimum in ω_t shows a dependence on the position of the ion temperature pedestal top. This dependence is also seen at low collisionality, however, no trend is seen for the density. Note that ω_t and T_i are measured with the same diagnostic, while ω_t and n_e are measured with two different diagnostics and the profiles need to be aligned radially. At low collisionality, the assumptions of the radial profile alignment used may not be applicable.

The results presented in this thesis show that the minimum in ω_t changes sign at low collisionality and the position of the minimum in ω_t is correlated with the position of the density and ion temperature pedestal tops.

Acknowledgements

First, I want to thank to Dr. Eleonora Viezzer, supervisor of this thesis, for giving me the opportunity to develop this work and for showing me how interesting the plasma physics can be.

Special thanks to Pilar Cano Megias, for the shared stay at Garching and for all the productive discussions about our master thesis.

I thank to all the Plasma Science and Fusion Technology (PSFT) group for the constant support and for the help received in the development of this work.

I finally thank to my family and Miriam, for always giving me good advice and the best of them.

Bibliography

[1] J. Wesson. *Tokamaks.* 3rd edition, ISBN 0 19 8509227, Oxford University Press, Oxford, 2004.

[2] EUROFUSION. *European Consortium for the Development of Fusion Energy.* URL http://www.euro-fusion.org/, 2017.

[3] F. Wagner *et al. Physical Review Letters*, 49(19):1408, 1982.

[4] T. Pütterich *et al. Physical Review Letters*, 102:025001, 2009.

[5] A.W. Leonard *et al. Physics of Plasmas*, 21:090501, 2014.

[6] H. Zohm *et al. Plasma Physics and Controlled Fusion*, 38:105–124, 1996.

[7] W. Suttrop. *Practical Limitations to Plasma Edge Electron Temperature Measurements by Radiometry of Electron Cyclotron Emission.* IPP Report 1/306, Max-Planck-Institute for Plasma Physics, Garching, Germany, 1997.

[8] S.K. Rathgeber *et al. Plasma Physics and Controlled Fusion*, 55:025004, 2013.

[9] B. Kurzan *et al. Review of Scientific Instruments*, 82:103501, 2011.

[10] J. Schweinzer *et al. Plasma Physics and Controlled Fusion*, 34(7):1173, 1992.

[11] M. Willensdorfer *et al. Review of Scientific Instruments*, 83:023501, 2012.

[12] O. Gehre. *International Journal of Infrared and Millimeter Waves*, 5(3), 1984.

[13] R.J. Fonck *et al. Physics Review A*, 29(6), 1984.

[14] E. Viezzer. *Radial electric field studies in the plasma edge of ASDEX Upgrade.* PhD thesis at Ludwig-Maximilians-Universität, Munich, 2012.

[15] E. Viezzer *et al.* *Plasma Physics and Controlled Fusion*, 53:035002, 2011.

[16] E. Viezzer *et al.* *Review of Scientific Instruments*, 83:103501, 2012.

[17] M. Cavedon *et al.* *Review of Scientific Instruments*, 88(4):043103, 2017.

[18] E. Wolfrum. *Conf. Proceedings of the 22nd IAEA Fusion Energy Conference*. EX/P3-7, Geneva, 2008.

[19] J. Neuhauser *et al.* *Plasma Physics and Controlled Fusion*, 44:869, 2002.

[20] A. Kallenbach *et al.* *Nuclear Fusion*, 43:573, 2003.

[21] P.A. Schneider *et al.* *Nuclear Fusion*, 53:073039, 2013.

[22] P.A. Schneider. *Characterization and scaling of the tokamak edge transport barrier.* PhD thesis at Ludwig-Maximilians-Universität, Munich, 2012.

[23] O. Sauter *et al.* *Physics of Plasmas*, 6:2834, 1999.

[24] M. Dunne *et al.* *Plasma Physics and Controlled Fusion*, 59:014017, 2017.

[25] E. Viezzer *et al.* *Nuclear Fusion*, 55:123002, 2015.